Софийски университет „Св. Климент Охридски"

Физически факултет

катедра „Атомна физика"

ДИПЛОМНА РАБОТА

Близък детектор от сцинтилационни влакна за Неутринната фабрика

Росен Иванов Матев

Научен ръководител:
доц. дфн Румен Ценов

София, 2011 г.

University of Sofia "St. Kliment Ohridski"

Faculty of Physics

Atomic Physics Department

Master Thesis

Scintillating fiber near detector for the Neutrino Factory

Rosen Ivanov Matev

Supervisor:

Assoc. Prof. Roumen Tsenov, Dr. Sc.

Sofia, 2011

Abstract

Neutrino Factory is a facility for future precision studies of neutrino oscillations. A so called near detector is essential for reaching the aimed precision of neutrino oscillation analysis. Main task of a near detector is to measure the flux of the neutrino beam. The brilliant neutrino source provides opportunity for precision studies of various neutrino interaction processes in a near detector. We present design concept of a scintillating fiber tracker capable of measuring the neutrino flux. The basic idea is to separate pure leptonic neutrino-electron scattering from the overwhelming background of neutrino-nucleon interactions. Monte Carlo simulation of the detector and simple event reconstruction algorithms are presented. It is shown that proper selection cuts increase signal to background ratio from $\sim 10^{-4}$ to 30-50 %. Two methods for extraction of signal events are developed.

Contents

List of Figures

List of Tables

Chapter 1

Introduction

Neutrino was postulated by W. Pauli in 1930 to explain the continuous kinetic energy spectrum of electrons in beta decay. He claimed that the hypothetical particle was carrying away energy, momentum and angular momentum, so that conservation laws are held. The direct observation of the neutrino was not until 1956, when F. Reines and C. Cowan conducted their experiment at the Savannah River nuclear reactor in South Carolina. It was using neutrinos generated by the reactor and measured the

$$\overline{\nu}_e + p \rightarrow e^+ + n \tag{1.1}$$

interactions with their unique signature.

1.1 Neutrino oscillations

1.1.1 History

The concept of neutrino oscillations was first stated in 1957 by B. Pontecorvo by analogy with the neutral kaons oscillations. The first observation of the phenomenon was made by R. Davis in the Homestake experiment in the late 1960s. The experiment counted the number of interactions of neutrinos emitted by nuclear fusion in the Solar core. Only one third of the theoretically predicted interaction rate was observed. Many subsequent experiments confirmed the deficit. In 2001, The Sudbury Neutrino Observatory provided the first direct evidence of solar neutrino oscillation. The experiment was able to detect solar neutrinos independently of flavor as well as only electron neutrinos. The measured

total flux of solar neutrinos agrees well with theoretical predictions, while electron neutrinos accounted for about 35 % of the total.

1.1.2 Phenomenology

To obtain a phenomenological description of neutrino oscillations one should abandon the Standard Model postulate of zero neutrino masses. In that case, neutrino mass eigenstates do not necessarily have equal eigenvalues and can in general not coincide with flavor eigenstates. Therefore, a flavor eigenstate of neutrino, $|\nu_\alpha\rangle$ ($l = e, \mu, \tau$), is in general expressed as superposition of mass eigenstates, $|\nu_i\rangle$ ($i = 1, 2, 3$):

$$|\nu_\alpha\rangle = \sum_i U_{\alpha i}|\nu_i\rangle, \tag{1.2}$$

where $U_{\alpha i}$ is an element of the Pontecorvo-Maki-Nakagawa-Sakata (PMNS) unitary matrix U. It is commonly parameterized with three mixing angles, θ_{12}, θ_{23} and θ_{13}, and one complex phase δ:

$$U = \begin{pmatrix} 1 & 0 & 0 \\ 0 & c_{23} & s_{23} \\ 0 & -s_{23} & c_{23} \end{pmatrix} \begin{pmatrix} c_{12} & s_{12} & 0 \\ -s_{12} & c_{12} & 0 \\ 0 & 0 & 1 \end{pmatrix} \begin{pmatrix} c_{13} & 0 & s_{13}e^{-i\delta} \\ 0 & 1 & 0 \\ -s_{13}e^{i\delta} & 0 & c_{13} \end{pmatrix}, \tag{1.3}$$

where $c_{ij} = \cos\theta_{ij}$ and $s_{ij} = \sin\theta_{ij}$. The evolution of an initial flavor eigenstate $|\nu_\alpha\rangle$ according to quantum mechanics is given by the superposition of the evolved mass eigenstates:

$$|\nu(t)\rangle = \sum_i U_{\alpha i}|\nu_i(t)\rangle = \sum_i U_{\alpha i}e^{-i(E_i t - p_i L)}|\nu_i\rangle, \tag{1.4}$$

where E_i and p_i are the energy and momentum of ν_i, and L is the traveled distance. Due to the smallness of the neutrino mass, we can make the following approximations:

$$t \approx L \tag{1.5}$$

$$E_i = \sqrt{p_i^2 + m_i^2} \approx p_i + \frac{m_i^2}{2p_i}, \tag{1.6}$$

where the natural units system ($\hbar = c = 1$) is used. The three mass eigenstates ν_i have the same momentum because ν_α is produced with a definite momentum $p \approx E$. The

probability that ν_β is observed after a distance L is given by

$$P(\nu_\alpha \to \nu_\beta) = |\langle \nu_\beta | \nu(t) \rangle|^2 = \left| \sum_i U_{\alpha i} U_{\beta i}^* e^{-i \frac{m_i^2 L}{2E}} \right|^2$$

$$= \delta_{\alpha\beta} - 4 \sum_{i>j} \mathrm{Re}(U_{\alpha i}^* U_{\alpha j} U_{\beta j}^* U_{\beta i}) \sin^2 \left(\frac{\Delta m_{ij}^2 L}{4E} \right)$$

$$\pm 2 \sum_{i>j} \mathrm{Im}(U_{\alpha i}^* U_{\alpha j} U_{\beta j}^* U_{\beta i}) \sin \left(\frac{\Delta m_{ij}^2 L}{2E} \right), \qquad (1.7)$$

where $\Delta m_{ij}^2 = m_i^2 - m_j^2$ is the mass squared difference between ν_i and ν_j, and "+" is for neutrinos and "-" is for antineutrinos. The independent square mass differences are only two because of the obvious relation $\Delta m_{12}^2 + \Delta m_{23}^2 + \Delta m_{13}^2 = 0$. Therefore, the parameters describing neutrino oscillations in general are six: three mixing angles, one complex phase and two squared mass differences. Experiments have observed oscillations in two distinct regions, one at approximately 30 times larger E/L than the other. Therefore, one mass splitting is much smaller than the other two: $\Delta m_{12}^2 \ll \Delta m_{23}^2 \approx \Delta m_{31}^2$. Because of this (and the smallness of $\sin\theta_{13}$), oscillations in the regions $E/L \sim \Delta m_{12}^2$ and $E/L \sim \Delta m_{23}^2$ can be approximated by oscillation of two neutrinos with effective mixing angle θ and squared mass difference Δm. The oscillation probability is then given by (for $\alpha \neq \beta$)

$$P(\nu_\alpha \to \nu_\beta) = \sin^2 2\theta \sin^2 \left(\frac{\Delta m^2 L}{4E} \right). \qquad (1.8)$$

1.2 Neutrino Factory

Neutrino Factory is a proposed facility for precise measurement of neutrino oscillation parameters. The Neutrino Factory will create an intense neutrino beam via decays of muons stored in racetrack-shaped storage rings. The decays of negative and positive muons

$$\mu^- \to e^- + \nu_\mu + \overline{\nu}_e \qquad (1.9)$$

$$\text{and} \quad \mu^+ \to e^+ + \overline{\nu}_\mu + \nu_e, \qquad (1.10)$$

provide two separate neutrino beams. The baseline layout of the accelerator complex is shown on Figure 1.1 [1]. Two detector locations are currently envisioned, one at "intermediate" (3000-5000 km) baseline distance and the other at "long"(7000-8000 km)
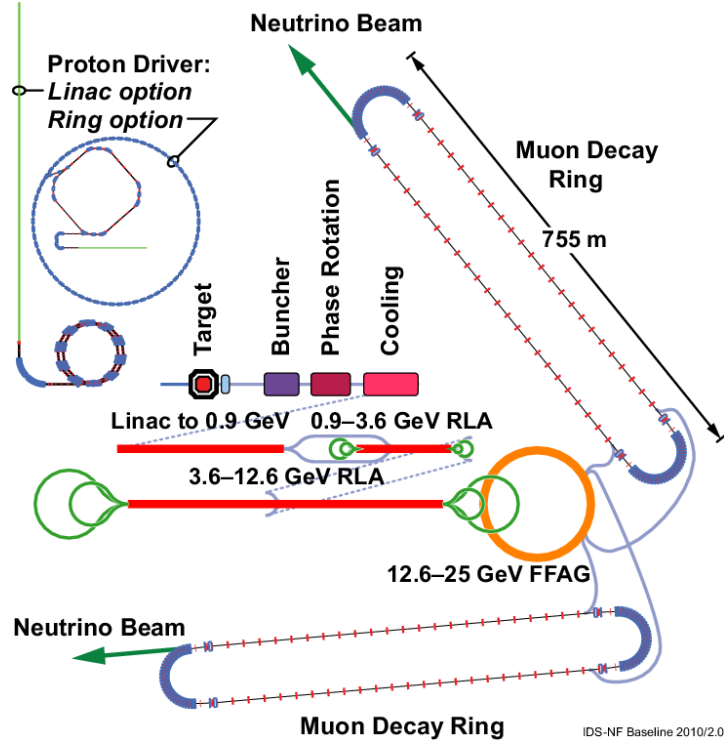
Figure 1.1: Baseline layout of the Neutrino Factory accelerator complex.

baseline distance. Specifications [1] give a total of 10^{21} useful muon decays for both signs and both detector locations for 10^7 s[1] useful time.

1.2.1 Accelerator complex

For achieving the baseline muon decays per year, a $4 \, MW$ primary proton beam is needed. The unprecedented beam power will be obtained by reusing and upgrading existing facilities and building new accelerators (linear or circular). The next step is to generate a secondary pion beam from interactions of the proton beam with a target. In order to avoid reinteractions of pions in the target, it has to be long and thin. This geometry imposes a great technical challenge due to the huge energy density created in the target. The solution being considered is a liquid jet mercury target [2]. Generated pions will be captured by a 20 T solenoid, which tapers down to 1.5 T in a distance of $15 \, m$. Contrary to a magnetic horn, the solenoid allows for both pion signs to be captured. The pion beam decays in a long decay channel, thus generating a tertiary muon beam with a large energy spread. The muons are bunched and phase-rotated in a sequence

---

[1]When "year" or "annual" is used further on, it refers to 10^7 s

of RF cavities so that a train of bunches with equal energies is formed. Following is a cooling channel, which reduces the transverse emittance of the muon bunches so that more muons fit in the acceptance of the following accelerators. Traditional techniques, such as stochastic, electron and laser cooling, are not applicable at the Neutrino Factory since they take in the order of seconds to minutes to cool a beam. Muons with a rest frame lifetime of 2.2 µs need to be cooled with a method that is fast enough. A novel approach is considered called ionization cooling. The idea behind the method is to use ionization losses to reduce emittance in both longitudinal and transverse directions and then accelerate to restore the initial momentum. A dedicated experiment called MICE [3] to prove the feasibility of the concept is in operation. Acceleration is divided into three stages, each chosen to use the most efficient acceleration method at its energy range. First, the muon beam is accelerated to 0.9 GeV energy by a linear accelerator. This is followed by two recirculating linear accelerators (RLA), which increase the energy of the beam to 3.6 GeV and 12.6 GeV, respectively. Finally the beam is accelerated in a fixed-field alternating-gradient (FFAG) accelerator. In both RLA and FFAG accelerators the beam makes many passes through the RF cavities, thus making them cost-effective solutions. The beam with an energy of 25 GeV is injected in two racetrack-shaped decay rings. They allow simultaneous storage of both muon signs. Each decay ring points toward one of the far detector locations.

1.2.2 Physics

The Neutrino Factory is the most promising future facility for studying of neutrino oscillation parameters. It has the following main goals:

- accurately measure $\sin^2(2\theta_{13})$ if it is relatively large, and have the potential to test very small values otherwise.[2]

- determine the hierarchy of neutrino mass eigenstates;

- measure the value of the CP violating phase δ.

The advantages of the Neutrino Factory compared to other present and future facilities are the intense flux, the ability to produce beams of both ν_μ ($\overline{\nu}_\mu$) and $\overline{\nu}_e$ (ν_e), the cleanliness of the beams. Twelve oscillation channels are available for studies. The six channels

---

[2]Recently, the T2K experiment has shown indication that $\sin^2(2\theta_{13})$ is large [4]. Best fits for normal and inverse hierarchies are 0.11 and 0.14, respectively. Statistical significance of the result is 2.5σ.

available in the $(\nu_\mu, \overline{\nu}_e)$-beam are shown in Table 1.1. The other six are their charge conjugates.

Table 1.1: Oscillation channels for a $(\nu_\mu, \overline{\nu}_e)$-beam ($\mu^-$ decay mode). Oscillation channels in the other decay mode are charge conjugates of these.

Channel	
$\nu_\mu \rightarrow \nu_e$	appearance "Platinum channel"
$\nu_\mu \rightarrow \nu_\mu$	disappearance
$\nu_\mu \rightarrow \nu_\tau$	appearance
$\overline{\nu}_e \rightarrow \overline{\nu}_e$	disappearance
$\overline{\nu}_e \rightarrow \overline{\nu}_\mu$	appearance "Golden channel"
$\overline{\nu}_e \rightarrow \overline{\nu}_\tau$	appearance "Silver channel"

The Golden channel $\nu_e \rightarrow \nu_\mu$ has a unique experimental signature of a muon with sign opposite to the muon signs in the decay ring. The channel gives opportunity for measuring both θ_{13} and δ parameters. However, there is an intrinsic degeneracy that continuously many solutions to the equation $P_{\alpha\beta}(\theta_{13}, \delta) = P$ exist. By studying both neutrino and anti-neutrino oscillations the continuous degeneracy can be eliminated. However, "intrinsic clone" degenerate solutions still remain. They arise from the lack of knowledge of the mass hierarchy and the octant where θ_{13} is located. These degeneracies can be resolved at the Neutrino Factory by studying different oscillation channels at two different baselines.

1.2.3 Near detector

A future neutrino facility will need near detectors in order to perform oscillation measurements with the required sensitivity. The near detector measurements that are essentialfor the neutrino oscillation analysis are [1]:

- measurement of neutrino flux;

- measurement of neutrino beam properties needed for the flux to be extrapolated to the far detector;

- measurement of charm production cross sections (charm production in far detectors is one of the principal backgrounds to the oscillation signal).

The brilliant neutrino beam allows for other standard neutrino physics studies, such as measurement of cross sections, structure functions and $\sin^2 \theta_W$ at neutrino energies in the 0-25 GeV range.

Chapter 2

Neutrino-electron scattering

Neutrino-electron interactions involve only fundamental particles, thus they do not depend on unknown form-factors. Cross sections of these processes are straightforwardly calculated in the Standard Model framework. Any small uncertainties could come only from well measured Standard Model parameters. Therefore, such processes are suitable for measurement of neutrino beam fluxes, provided that beams are intense enough. The cross sections given in this chapter are calculated in the low-energy approximation with four-fermion interaction. This approximation is justified for interactions with $s \ll m_{\mathrm{W}}^2$. For a Neutrino Factory beam having maximum energy of $E_\nu = 25$ GeV, the square of the invariant mass is

$$s = (p_\nu + p_{\mathrm{e}})^2 = 2E_\nu m_{\mathrm{e}} + m_{\mathrm{e}}^2 \approx 0.03 \text{ GeV}^2. \tag{2.1}$$

Neutrino-electron interactions relevant for a Neutrino Factory beam are briefly described in the following sections.

2.1 Quasi-elastic scattering

The two purely leptonic interactions of neutrinos from the Neutrino Factory beam producing a muon in final state are

$$\nu_\mu + \mathrm{e}^- \to \mu^- + \nu_{\mathrm{e}} \tag{2.2}$$

$$\text{and} \quad \overline{\nu}_{\mathrm{e}} + \mathrm{e}^- \to \mu^- + \overline{\nu}_\mu. \tag{2.3}$$

8

The process in equation (2.2), known as inverse muon decay, has an isotropic differential cross section in the center of mass frame. The total cross section is given by [5]

$$\sigma = \frac{G_F^2}{\pi} \frac{(s - m_\mu^2)^2}{s},$$
(2.4)

where G_F is the Fermi coupling constant, s is the square of the invariant mass of the system and m_μ is the mass of the muon. The process in equation (2.3), known as muon production through annihilation, has differential cross section in the center of mass frame given by [5]

$$\frac{d\sigma}{d\cos\theta} = -\frac{G_F^2}{2\pi} \frac{(s - m_\mu^2)^2}{s^2} \left(E_{\mathrm{e}} + E_{\bar{\nu}_{\mathrm{e}}} \cos\theta\right) \left(E_\mu + E_{\nu_\mu} \cos\theta\right)$$
(2.5)

and the total cross section is

$$\sigma = \frac{G_F^2}{\pi} \frac{(s - m_\mu^2)^2}{s^2} \left(E_{\mathrm{e}} E_\mu + \frac{1}{3} E_{\bar{\nu}_{\mathrm{e}}} E_{\nu_\mu}\right).$$
(2.6)

The neutrino energy threshold (for electrons at rest) for both processes is

$$E_\nu \geq \frac{m_\mu^2 - m_{\mathrm{e}}^2}{2m_{\mathrm{e}}} \approx 10.9 \text{ GeV}.$$
(2.7)

The two quasi-elastic neutrino-electron scattering processes will be referred to with IMD.

2.2 Elastic scattering

There are two pure neutral current reactions of interest:

$$\nu_\mu + \mathrm{e}^- \to \nu_\mu + \mathrm{e}^-$$
(2.8)

$$\text{and} \quad \bar{\nu}_\mu + \mathrm{e}^- \to \bar{\nu}_\mu + \mathrm{e}^-.$$
(2.9)

Their respective cross sections are [6]

$$\sigma(\nu_\mu \mathrm{e} \to \nu_\mu \mathrm{e}) = \frac{G_F^2 m_{\mathrm{e}} E_\nu}{2\pi} \left(1 - 4\sin^2\theta_W + \frac{16}{3}\sin^4\theta_W\right) \quad \text{and}$$
(2.10)

$$\sigma(\bar{\nu}_\mu \mathrm{e} \to \bar{\nu}_\mu \mathrm{e}) = \frac{G_F^2 m_{\mathrm{e}} E_\nu}{2\pi} \left(\frac{1}{3} - \frac{4}{3}\sin^2\theta_W + \frac{16}{3}\sin^4\theta_W\right),$$
(2.11)

where θ_W is the Weinberg angle and $E_\nu \gg m_e$ approximation was made. The other processes of interest result from both $W^\pm$ and Z^0-boson exchange:

$$\nu_e + e^- \rightarrow \nu_e + e^- \tag{2.12}$$

$$\text{and} \quad \overline{\nu}_e + e^- \rightarrow \overline{\nu}_e + e^-. \tag{2.13}$$

Their respective cross sections are [6]

$$\sigma(\nu_e e \rightarrow \nu_e e) = \frac{G_F^2 m_e E_\nu}{2\pi}\left(1 + 4\sin^2\theta_W + \frac{16}{3}\sin^4\theta_W\right) \quad \text{and} \tag{2.14}$$

$$\sigma(\overline{\nu}_e e \rightarrow \overline{\nu}_e e) = \frac{G_F^2 m_e E_\nu}{2\pi}\left(\frac{1}{3} + \frac{4}{3}\sin^2\theta_W + \frac{16}{3}\sin^4\theta_W\right). \tag{2.15}$$

The elastic neutrino-electron scattering processes will be referred to with ES.

2.3 Experimental signatures

Total cross sections for neutrino-electron interactions as a function of neutrino energy are given on Figure 2.1. Despite their smallness, a couple of tons detector placed 100 m after the straight section end can provide sufficient interaction rate - Figure 2.2. However, inclusive charged current (CC) and neutral current (NC) neutrino interactions with nuclei

$$\nu_\ell + N \rightarrow \ell + X \tag{2.16}$$

$$\text{and} \quad \nu_\ell + N \rightarrow \nu_\ell + X \tag{2.17}$$

are a few orders of magnitude more frequent. For example, muon neutrino and anti-neutrino CC total cross sections in DIS regime are [7] $\sigma/E_{\nu_\mu} \approx 0.68 \times 10^{-38}$ cm^2/GeV and $\sigma/E_{\overline{\nu}_\mu} \approx 0.33 \times 10^{-38}$ cm^2/GeV respectively. At 15 GeV the muon neutrino CC total cross section is $\sim 1 \times 10^{-37}$ cm^2, compared to $\sim 2 \times 10^{-41}$ cm^2 for inverse muon decay $\nu_\mu e^- \rightarrow \mu^- \nu_e$. An obvious distinction between purely leptonic processes and processes (2.16) and (2.17) is the lack of hadronic system X in the former. Measurement of the recoil energy of the hadronic system can be used as good criterion for background suppression. Muons from quasi-elastic neutrino-electron scattering have a distribution peaked at very forward direction. At the Neutrino Factory, the polar angle of IMD muons does not exceed 5 mrad. The angular spread comes mainly from the intrinsic scattering angle ~ 4 mrad in processes (2.2) and (2.3), while neutrino beam divergence
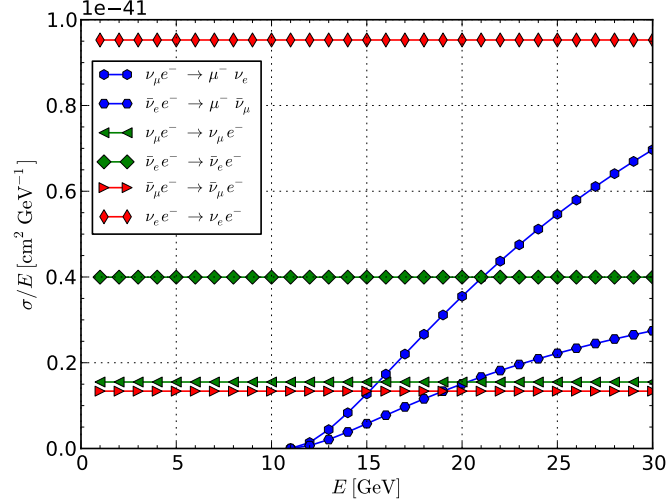
Figure 2.1: Total cross section divided by neutrino energy for the leptonic interactions in a Neutrino Factory beam. Blue and green show processes which occur with μ^- in the storage ring, while red shows processes which occur with μ^+ in storage ring. Hexagon markers show CC interactions, triangle markers show NC interactions and rhombus markers show mixed CC+NC interactions. The threshold for quasi-elastic processes (blue) is evident at $\sim 11\ GeV$.

(and solid angle covered by detector) has little contribution. This kinematic property can be used as another event selection criterion. Polar angle distribution of electrons from neutrino-electron elastic scattering is ten times wider and is not suitable for event selection. On the other hand, the $\theta_\ell^2 E_\ell$ variable[1], provides good separation between signal and background for all neutrino-electron scattering processes.

---

[1]The variable $\theta_\ell^2 E_\ell$ is proportional to Bjorken's $y = 1 - E_\ell/E_\nu$ (event inelasticity) for elastic and approximately proportional for quasi-elastic scattering.
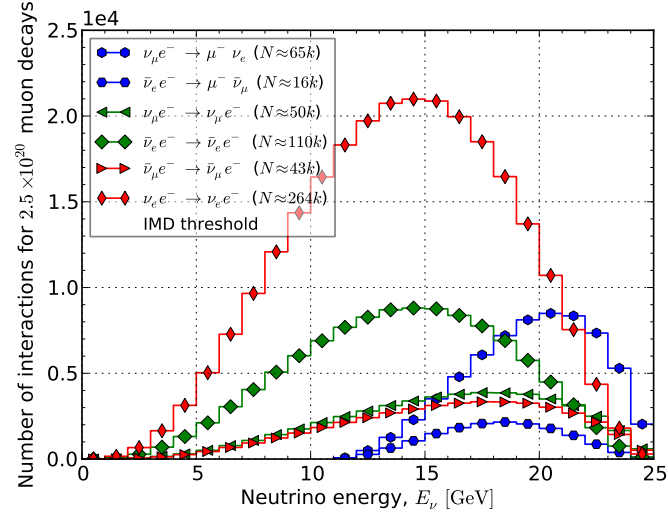
Figure 2.2: Number of neutrino-electron interactions for a nominal year of Neutrino Factory operation. Rates are calculated for 2.7 t detector with 1.5×1.5 m^2 frontal cross section and average $Z/A \approx 0.54$. Detector is placed 100 m after the straight section end. Dashed vertical line indicates threshold for quasi-elastic scattering.

Chapter 3

Near detector

3.1 Measurement of neutrino-electron scattering

To perform measurements of neutrino-electron scattering, the detector must be able to distinguish between the leptonic interactions and inclusive CC and NC neutrino interactions (2.16) and (2.17), which are a few orders of magnitude more frequent. To accomplish this task, the detector must make use of the distinctive event signatures mentioned in Section 2.3. This imposes certain general requirements to the design of the near detector. It should be/have:

- massive enough to provide sufficient interaction rate;

- tracker-like design to measure precisely the primary lepton's scattering angle;

- magnetic field to measure the momentum of the primary lepton;

- precise calorimeter to separate background events based on hadronic recoil energy;

- low Z material to minimize multiple scattering and electromagnetic showering.

3.2 Scintillating fiber tracker

A detector design which fulfills the requirements stated in Section 3.1 is proposed. The detector design is essentially a scintillating fiber tracker with an incorporated calorimeter. A schematic drawing of the detector[1] is shown on Figure 3.1. A right-handed coordinate

---

[1]From now on, the scintillating fiber tracker will be referred to as "the detector".
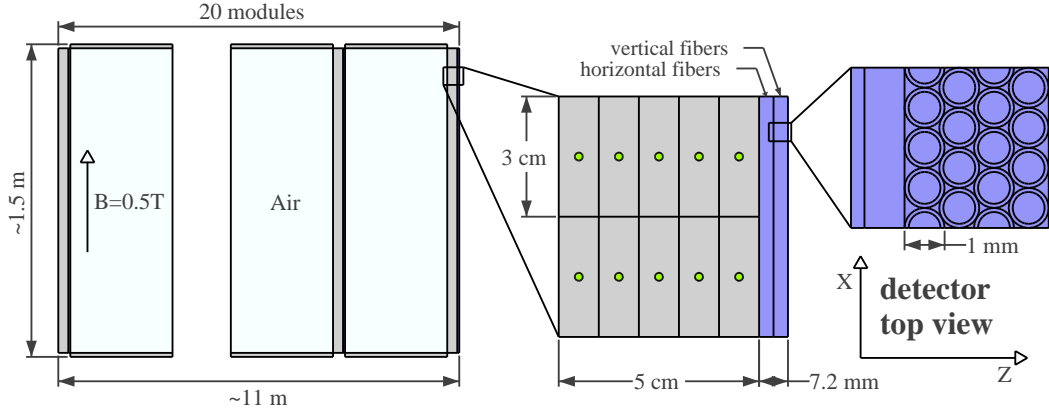
Figure 3.1: Schematic drawing of the detector.

system is adopted in which the origin is at the most upstream surface of the detector, the positive Z axis is aligned with the neutrino beam axis and the positive Y axis is pointing upwards. The detector consists of 20 square shaped modules placed perpendicular to the beam axis. Each module has a calorimeter section and a tracker section (also called tracker station). Modules are positioned equidistantly forming gaps filled with air. With larger distance between tracker stations, transverse displacement of hits is increased and thus angular resolution improved. The sides of the air gaps are covered with a layer of plastic scintillating bars. These layers are referred to as *side slabs*. The detector is placed in 0.5 T dipole magnetic field. Each station consists of one layer of fibers with horizontal orientation and another with vertical orientation. Each layer has four planes made of 1 mm round fibers. They form a hexagonal pattern in the layer, thus minimizing dead volume. Calorimeter sections consist of plastic scintillating bars arranged in 5 slabs. All bars are oriented vertically, so that their axes are perpendicular to the magnetic field vector. Bars are co-extruded with a wavelength shifting (WLS) fibers inside and have 10 mm by 30 mm cross-section. Both tracker fibers and WLS fibers in bars are read from both ends by silicon photomultipliers (SiPMs). Overall dimensions of the detector are $\sim 1.5\,\text{m} \times 1.5\,\text{m} \times 11\,\text{m}$. The detector mass is $\sim 2.7\,\text{t}$.

3.3 Silicon photon detectors

SiPM photo detectors combine many small avalanche photodiodes operated in Geiger mode to form a single device (see Figure 3.2). They were proposed in the 1990s [8,9]. Detailed information about SiPMs can be found in a recent review paper [9]. In the past
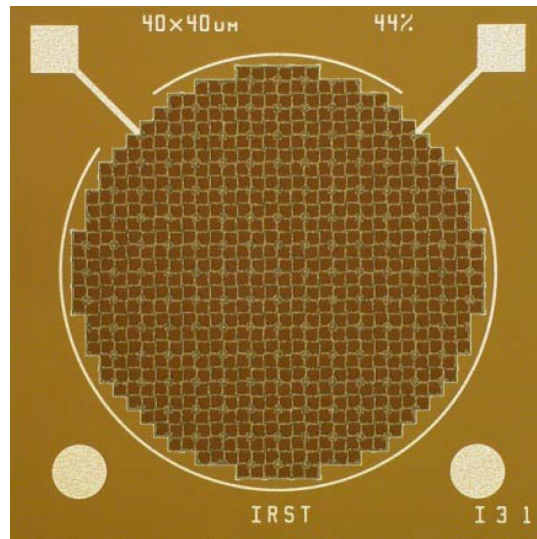
Figure 3.2: Photograph of 1.2 mm diameter SiPM manufactured in FBK, Trento, Italy.

several years the technology has undergone rapid development, making it competitive to conventional photomultiplier tubes (PMT). Advantages of SiPMs over PMTs are numerous and include: independence of external magnetic fields, high photon detection efficiency, low operating voltage, compact size. The most important advantage is that SiPMs can be manufactured in standard microelectronics facilities. Furthermore, it is possible to integrate electronics into the SiPM itself, lowering the cost per channel. This makes silicon photomultipliers especially suitable for application in detectors having hundreds of thousands fibers, such as the scintillating fiber tracker. A SiPM device is build from array of avalanche photodiodes (pixels). Size of pixels varies from 20 µm to 100 µm. Each avalanche photodiode is operated in Geiger mode, meaning that a primary trigger (photon, thermal electron) creates a discharge in the pixel. This results to a gain in the order of 10^6. Each pixel is rearmed by a resistor which quenches the discharges by the voltage drop induced from the discharge current. All pixels are connected in parallel, thus forming an analog signal which is a sum of all pixel signals. Therefore, the SiPM signal is proportional to the number of primary triggers, provided that it is not saturated. Although the SiPM acts as an analog device, in the case of few incident photons, the signal exhibits the discrete structure of the device, because all pixels are nearly the same. The operating voltage is in the 25-70 V range, a few volts above the diode's breakdown voltage.

The photon detection efficiency (PDE) of a SiPM depends on three factors:

$$\mathrm{PDE} = QE \times \varepsilon_{pt} \times \varepsilon_{geom}, \tag{3.1}$$

where QE is the wavelength dependent quantum efficiency, ε_{pt} is the probability of initiating a Geiger discharge by a primary trigger and ε_{geom} is the sensitive fraction of the device area. The gain of SiPMs is voltage dependent and varies across different production sets of the same device. Moreover, gain has also a temperature dependence, which additionally complicates calibration procedures. Discharges induced by thermal electrons are called dark counts. Dark count rate is temperature dependent and has a typical value of less than 1 MHz for 1 mm^2 devices at room temperature. When single photon counting is not essential, imposing a threshold on the signal can eliminate most of the dark counts.

Chapter 4

Monte Carlo simulation

4.1 Neutrino beam simulation

Neutrino flux at the near detector is generated by a Monte Carlo simulation of muon decays along the straight section of the NF decay ring [10, 11]. This Section will briefly discuss the simulation.

For the decay of the negative muon, the expected decay distribution for the Standard Model values of Michel parameters is [12]

$$\frac{d^2\Gamma}{dx\, d\cos\theta} \sim x^2((3-2x) + P_\mu \cos\theta(1-2x)) \quad for\ \nu_\mu, \tag{4.1}$$

$$\frac{d^2\Gamma}{dx\, d\cos\theta} \sim x^2((1-x) + P_\mu \cos\theta(1-x)) \quad for\ \overline{\nu}_e, \tag{4.2}$$

where $x = 2E_\nu/m_\mu$, P_μ is the muon polarization and θ is the angle between the muon polarization vector and the direction of the neutrino. For the decay of the positive muon, the sign of the term containing $\cos\theta$ should be inverted. Energy and angular $(\tan^{-1}(dx/dz))$ distributions of muons in the beam are taken to be Gaussian. It is assumed that the transverse distribution of muons in the beam pipe is a Dirac delta function. The parameters used for the beam simulation are given in Table 4.1.

The simulation of each muon decay goes as follows. First, a position of the decay along the straight section is drawn from a uniform distribution. Then, for each neutrino, x and $\cos\theta$ is drawn from distributions 4.1, 4.2 using the acceptance-rejection method. An azimuthal angle ϕ is drawn from uniform distribution. Having x, $\cos\theta$ and ϕ, the momentum of the neutrino in the center of mass (CM) frame of the muon is obtained.

Table 4.1: Parameters of the beam in the muon storage ring used in the simulation.

Parameter	Value
Muon energy central value	25 GeV
Muon energy RMS	80 MeV
Muon angular spread	0.5 mrad
Muon polarization	0
Straight section length	600 m
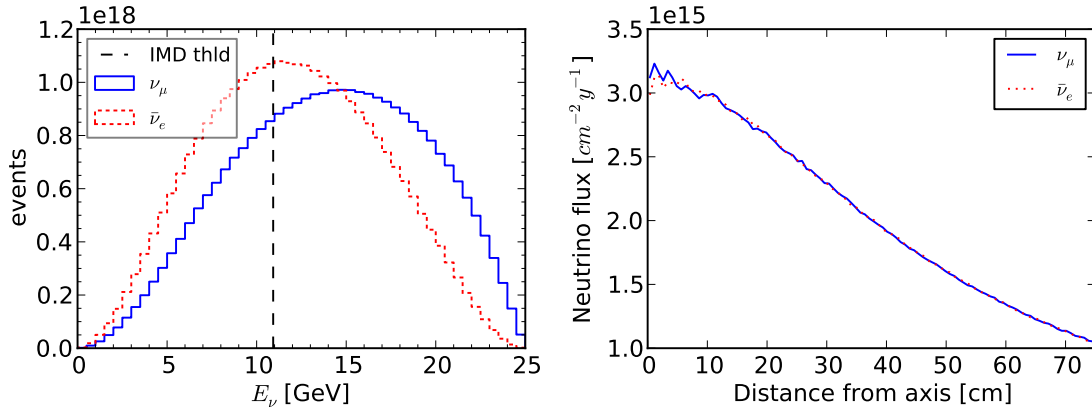
Figure 4.1: Energy spectrum (left) and radial distribution (right) of neutrinos on plane perpendicular to the straight section and 100 m away from its end. The distributions are normalized to the baseline specification of 2.5×10^{20} muon decays per muon charge per straight section. Dashed line indicates the threshold for the leptonic processes with muon in the final state.

Energy and polar angle of the muon are drawn from the according Gaussian distributions. Combining with an uniform random azimuthal angle, one obtains the muon momentum vector in laboratory frame. The neutrino momenta vectors in the CM frame are boosted to obtain the momenta in the laboratory frame. Electrons (positrons) from the decay are not simulated.

The most upstream plane of the near detector is to be situated at 100 m after the straight section end. The energy and space distributions of neutrinos at that plane is shown on Figure 4.1.

4.2 Neutrino interactions

The neutrino interactions with nuclear targets and electrons is simulated with the GENIE neutrino Monte Carlo generator [13]. The following neutrino interaction processes are simulated by GENIE:

- Quasi-elastic scattering;

- Elastic NC scattering;

- Baryon resonance production in charged and neutral current interactions;

- Coherent neutrino-nucleus scattering;

- Non-resonant deep inelastic scattering;

- Quasi-elastic charm production;

- Deep-inelastic charm production;

- Neutrino-electron elastic scattering; and

- Inverse muon decay.

The process $\overline{\nu}_e + e^- \rightarrow \overline{\nu}_\mu + \mu^-$ is not included in GENIE. For the simulated beam, the process above gives 4 times less interactions than inverse muon decay as can be seen from Figure 2.2. For this work GENIE version 2.6.2 has been used. Configuration was changed, so that short-lived charm particles are decayed by GENIE. Apart from this change, default values were used for all other parameters.

The NF neutrino flux is fed to GENIE by implementing a flux driver interface. The detector description used for event generation is a simplified version of the actual detector geometry. Each detector module is implemented as a solid box made of polystyrene. Air gaps are left as they are. Covering side bars are not implemented as interactions there are not in fiducial volume. For each neutrino interaction, GENIE produces a list of intermediate and final state particles with their kinematic characteristics. The type of the process involved in the interaction as well as some kinematic variables are also provided.

4.3 Detector simulation

4.3.1 Particle transport

For the simulation of detector response to neutrino interactions, the Geant4 [14,15] software platform was used. Geant4 is a toolkit for "the simulation of the passage of particles through matter". From the user's point of view, to simulate an event with Geant4 one has to define (by implementing the toolkit's interface classes):

- primary particle generator;

- list of particles to be transported (including decay products and particles produced in interactions) through the detector and relevant physics processes (physics list);

- detector description in terms of geometric volumes and comprising materials;

- "sensitive" volumes, where "snapshots" of the physical interaction and state of particles are recorded to produce "hits".

All final state particles produced by GENIE are passed to Geant4 simulation as primary particles. The physics list used in the simulations is "Simple and Fast Physics List" [16]. The scintillating fiber tracker geometry was implemented in a flexible manner, so that detector parameters are set with a configuration file. Plastic scintillating fibers and bars are defined as sensitive volumes. The hits produced in sensitive volumes contain: unique id of the volume, id of the particle, energy deposition, time and position of the interaction. True particle trajectories are recorded for some of the particles. Part of the information recorded in the simulation is used to produce electronic signals (digitization). Other data is retained for later comparison of reconstructed data with true data (often called "Monte Carlo" truth). By doing the comparison with MC truth, the performance of the detector design and reconstruction algorithms can be analyzed. A basic event display has been developed to enable visual inspection of events. Part of an example event display is shown on Figure 4.2. Apart from MC truth, the event display shows some reconstructed data.

Tracking of individual particles with Geant4 is stopped when their energy is below a certain threshold and it is guaranteed that they will not cross a volume border. Scintillation process was not included in the Geant4 simulation because tracking of individual scintillating (optical) photons is a very time consuming task.
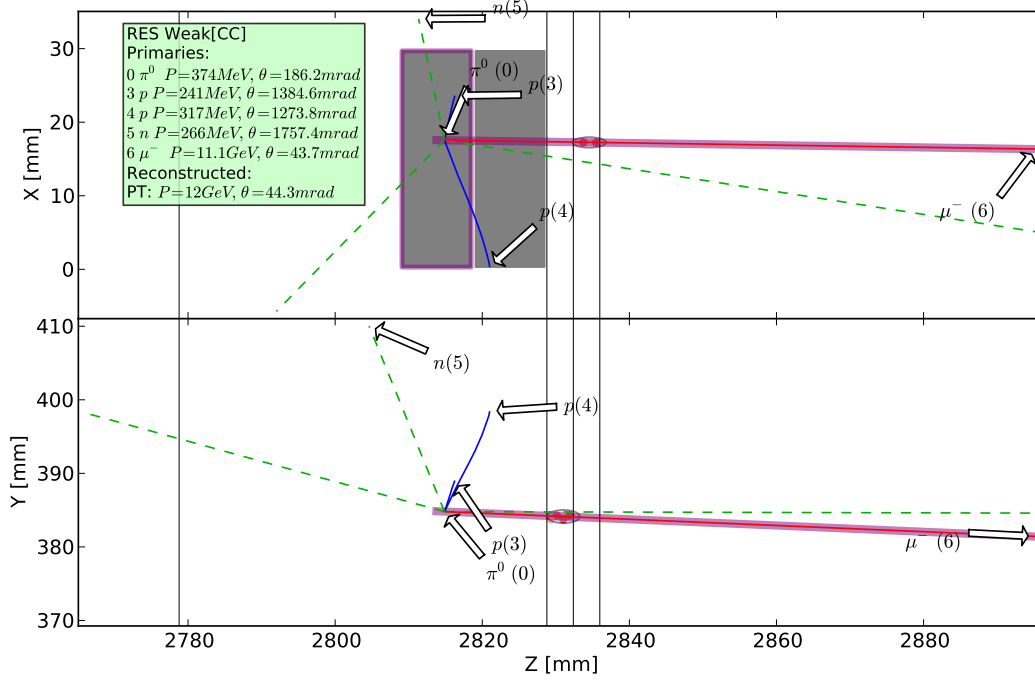
Figure 4.2: Example event display showing a CC resonance production event.

4.3.2 Digitization

Digitization algorithms take the output hits of the Geant4 simulation and transform them into electronic signals.

Fiber signal digitization

As simulation of optical photons is not feasible in event by event basis, a toy Monte Carlo algorithm was developed to simulate the processes of scintillation, photon propagation into fibers and SiPM response. For each energy deposit in a fiber, a random number of scintillating photons is drawn according to the scintillation yield of the material. The scintillating photons are emitted isotropically, hence not all of them suffer total internal reflection from the walls of the fibers. The fraction of photons which do not exit the fiber is called trapping efficiency. It is determined from refraction indexes and fiber cross-section. For round fibers manufacturers provide a "minimal" trapping efficiency, namely the efficiency for photons propagating in a single central plane. However, it has been shown [17] that the real trapping efficiency is about two times higher than that. A value of 8 % for the trapping efficiency is used in the simulation. The trapping efficiency

and light attenuation are taken into account to produce a number of photons arriving at the end of the fiber. If there are multiple hits in a fiber, photons arriving at the fiber end are summed up. The obtained number of photons is multiplied with an optical coupling efficiency factor to get the number of incident photons on the SiPM surface. Multiplying the last number by the photon detection efficiency (PDE) one obtains the number of primary avalanche triggers. Dark counts are simulated by further adding a Poisson distributed number to the primary triggers. The final electronic signal response is parameterized by a function that takes into account cross-talk effect and the single pixel response distribution. Only signals with amplitude larger than threshold equivalent to 2.5 fired pixels are recorded. For each fiber, the signals from both photo detectors and an id of the fiber are stored in a structure called *fiber digit* only if both signals are above the threshold. It seems dark counts are not a major problem for 1 mm fibers and modern SiPMs, which have less than 1 MHz/mm^2 dark count rate at room temperature. With the imposed signal threshold and coincidence requirement the number of "false" fiber digits is under 1 % of all fibers in the detector. Therefore, the probability to have two or more adjacent "false" fiber digits which mimic true particle hits is negligible.

Bar signal digitization

As above, Geant4 simulation does not treat optical photon processes in the scintillating bars and the WLS fibers inside. Ideally, one can make a detailed simulation or an experiment with prototype bar and parameterize the signal response (wavelength spectrum) at the end of the WLS fiber. However, we do not have such parameterization. For this work, bar signals were naively digitized by smearing energy deposits with 20 % Gaussian. Signals below a threshold of 0.5 MeV equivalent are discarded. For each bar, the signals from both photo detectors and an id of the bar are stored in a structure called *bar digit*.

Chapter 5

Software reconstruction

Raw output from both Monte Carlo simulation and a real experiment is a set of digitized signal amplitudes. To understand what processes took place and what particles propagated through the detector, one needs to obtain measurements of relevant physical quantities characterizing them. The aim of reconstruction algorithms is to infer high level information about the event from the raw detector output.

5.1 Initial processing

The first step of reconstruction process is to obtain some basic physical quantities from the digital signals. First, signal from the photo detectors should be translated back to number of incident photons. For fibers in tracker stations this quantity is sufficient. On the other hand, for bars, one should further obtain an absolute measurement of the energy deposit via a dedicated calibration procedure. Since this is a simulation rather than real experiment, the above procedure is assumed perfect and the calibration step is skipped.

To simplify further the reconstruction, neighboring fired fibers are grouped into clusters. Two fibers are considered neighbors if their projections on the XY plane are either neighboring or overlapping. Depending on the fibers orientation, (x, z) or (y, z) position of the cluster is calculated by taking weighted average of the fiber positions. Weighted standard deviations from the mean coordinates are also calculated. A cluster object then contains list of fibers, two coordinates with their standard deviations and an amplitude, which is the sum of the numbers of incident photons on the photo detectors
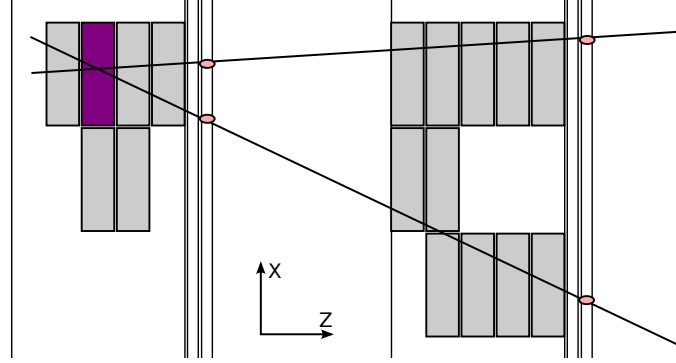
Figure 5.1: Vertex volume reconstruction example. The two adjacent most upstream stations with at least one cluster each are considered. The clusters (pink ellipses) with highest X coordinate are selected from both stations and a line passing through their centers is taken. Another line is constructed from the clusters with lowest X coordinates. The most upstream fired bar, which is between the lines (but not upstream of the intersection point) is identified as vertex bar (purple box).

at the fibers. Clusters composed of only one fiber are discarded to eliminate false hits due to SiPM noise.

5.2 Vertex reconstruction

The point where a neutrino interaction takes place is called vertex. The scintillating fiber tracker, like a typical neutrino detector, serves as a target. Therefore, one does not have *a priori* knowledge of the precise vertex coordinates. The vertex reconstruction algorithm attempts to find the volume (bar or fiber), where the vertex is located. Only the two most upstream stations with at least one cluster are considered. Since particle tracks are not curved in the XZ plane, we can linearly back-project the positions of the clusters towards the event vertex. To do this, the clusters with highest X coordinate are selected from both stations and a line passing through their centers is taken. Another line is constructed from the clusters with lowest X coordinates. The most upstream fired bar, which is between the lines (but not upstream of the intersection point) is identified as vertex bar (Figure 5.1). If there is no such bar, the cluster with the highest amplitude in the first upstream station is picked and its most upstream fiber is labeled as vertex volume. If there are no two adjacent stations with at least one cluster in each, the vertex cannot be reconstructed and the event is discarded. 86 % of the events have their vertex volume reconstructed.
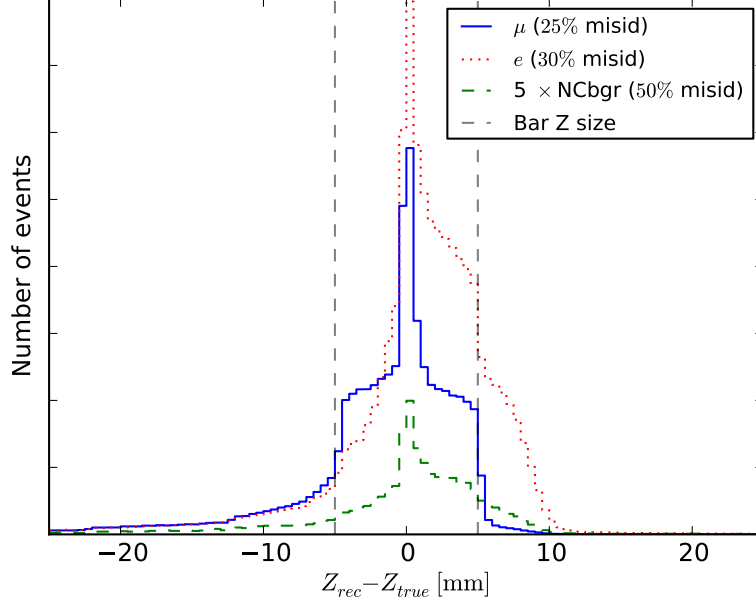
Figure 5.2: Vertex Z coordinate resolution. Distributions of the difference of reconstructed and true vertex Z coordinate are shown for CC ν_μ interactions (solid blue), CC $\overline{\nu}_e$ interactions (dotted red) and NC (ν_μ, $\overline{\nu}_e$) interactions (dashed green, $\times 5$). Vertical dashed lines indicate Z boundaries of a bar centered at 0. Uniform distribution of events with correctly identified vertex bar is clearly visible. Events in the narrow peak centered at 0 have their vertex volume correctly identified in a cluster. The shoulder on the right (and the dip left of 0) for CC $\overline{\nu}_e$ interactions (red) correspond to events with a reconstructed vertex bar adjacent and downstream of the true vertex bar. This misidentification may be explained with energy deposition in the vertex bar below the threshold and is only visible in antineutrino events. Misidentification probabilities for the three samples are shown in the legend.

However, the vertex volume is not always correctly identified. The performance of the algorithm is shown on Figure 5.2 in terms of difference between Z coordinate of the reconstructed volume's center and the true vertex Z coordinate. Difference distributions are shown for interactions of (ν_μ, $\overline{\nu}_e$)-beam.

5.3 Primary track reconstruction

The scintillating fiber tracker is a very fine grained detector. Because of this, reconstruction of the full event topology might be attempted. However, for the purpose of measuring purely leptonic processes, only events with a single track originating from the

vertex are considered. The main goal of reconstruction is to identify the *primary (lepton) track* and measure its parameters.

Only events with one cluster per orientation in the first two stations are considered. This selection has low efficiency, because an event with a single primary particle might still have more than one cluster in the either of the first stations. (Consider δ-electrons or interactions of bremsstrahlung photons) Furthermore, as both angle and momentum of the primary track need to be measured, only events with hits in at least three tracker stations are retained. The remaining fraction of leptonic events after the above selections is 61 % for IMD and 52 % for ES. Angle and curvature of tracks is measured using only hits in the first three stations. In third station, if there are more than one clusters, only the cluster nearest to the straight line defined by clusters in the first two stations is considered. At the end, for the primary track we have: initial position, initial slopes ($x_0' = dx/dz$ and $y_0' = dy/dz$), initial momentum and charge.

To asses the performance of the primary track reconstruction algorithm, the reconstructed track initial angles and momenta are compared to MC truth. Distribution of difference between reconstructed initial angle of the primary track θ_{rec} and true initial angle of the primary lepton θ_{true} is shown on Figure 5.3. From the Gaussian fit to the distribution, it is seen that the reconstructed angle is unbiased and the resolution (σ parameter of the fit) is ~ 0.5 mrad for both muons and electrons. Distribution of relative difference between reconstructed initial momentum of the primary track and true initial momentum of the primary lepton

$$\Delta = \frac{p_{rec} - p_{true}}{p_{true}}, \tag{5.1}$$

is shown on Figure 5.4. For muons, the Gaussian fits show that the reconstructed momentum have only small bias (due to energy loss) and resolution is going up to ~ 9 % for the highest energy muons. For electrons, the distribution is biased towards the negative values with a heavy negative tail. The reason for this underestimation of electrons' initial momenta is that they loose momentum due to bremsstrahlung and ionization. If energy loss is taken into account with Kalman filter fitting, for instance, bias can be reduced. Kalman filter fitting [18] is a powerful method, which can improve angular and momentum resolutions. This is true especially if full advantage of pattern recognition abilities of the method are used.
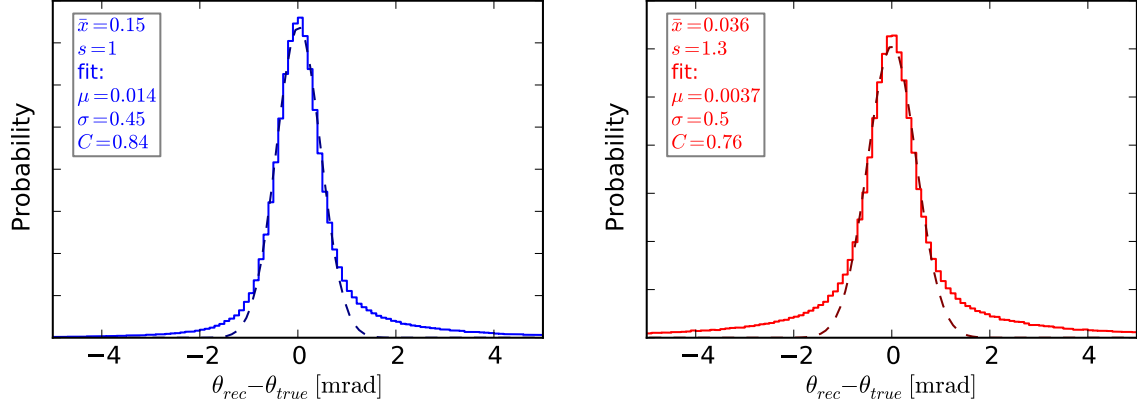
Figure 5.3: Obtained angular resolution for muons (left) and electrons (right). Gaussian fits are shown with dashed lines. The sample mean, standard deviation and the fit parameters are shown in upper left corners.
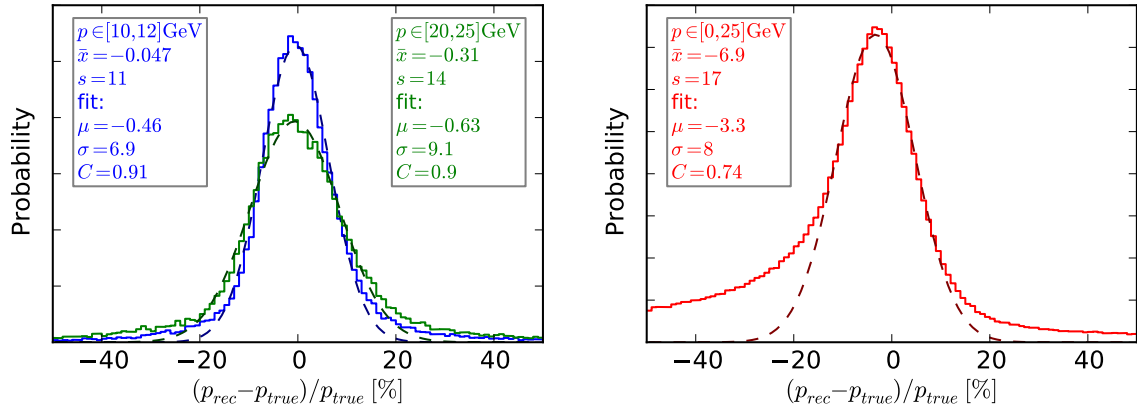

Figure 5.4: Obtained momentum resolution for muons (left) and electrons (right). Gaussian fits are shown with dashed lines. The sample mean, standard deviation and the fit parameters are shown in upper corners. For muons, distribution is shown for two samples of events: one with true muon momentum in the [10-12] GeV range (blue) and one in the [20-25] GeV range (green).

5.4 Spatial distribution of energy deposits

Having this rather simple event reconstruction, a backward going particle will cause wrong reconstruction of vertex position. Moreover, the backward going track will be wrongly identified as a primary lepton track. Some background events have particles which do not cross the first tracker station after the vertex and do not deposit enough energy in the vertex volume. In order to select events with a single primary particle one might exploit the spatial symmetry of energy deposits relative to the track. A variable which has good signal/background event separation power is the following. Firstly, we calculate the energy deposit weighted average position of the hits in the bars in the i-th slab:

$$x_i^{obs} = \frac{\sum_j x_{ij} \Delta E_{ij}}{\sum_j \Delta E_{ij}}, \tag{5.2}$$

where j denotes the bar in the slab, x_{ij} is the X coordinate of the center of the bar and ΔE_{ij} is the energy deposit in the bar. Secondly, the expected position of the primary track at the i-th slab is calculated:

$$x_i^{exp} = x_0 + x_0'(z_i - z_0), \tag{5.3}$$

where z_i is the Z coordinate of the i-th slab's center, x_0 and z_0 are the primary track's initial coordinates and $x_0' = dx/dz$ is the primary track's initial slope. Finally, the variable is

$$x_{dev} = \frac{1}{n} \sum_i |x_i^{obs} - x_i^{exp}|, \tag{5.4}$$

where the summation is over all fired slabs. Such variable is expected to have low values for events with a single muon, medium values for electron showers and high ones for high multiplicity asymmetric events.

Overall reconstruction efficiency (remaining signal events) is 53 % for IMD and 45 % for ES. Inefficiencies come from inability to reconstruct the vertex, selection of events based on the number of clusters in the two most upstream fired stations and inability to reconstruct primary track's initial angle and momentum.

Chapter 6

Data analysis

6.1 Neutrino-electron scattering event selection

The Neutrino Factory beam is composed of ν_μ and $\overline{\nu}_e$ neutrinos in μ^- decay mode and from $\overline{\nu}_\mu$ and ν_e neutrinos in μ^+ decay mode. Since we can distinguish interactions only by their final state, we should group neutrino-electron interactions as follows: processes (2.2) and (2.3) in the *IMD* group; processes (2.8) and (2.13) in the ES^- group; processes (2.9) and (2.12) in the ES^+ group. Sometimes *ES* will be used when referring to both ES$^-$ and ES$^+$. Three neutrino-electron event samples are selected from all events corresponding to the three groups. IMD and ES$^-$ samples are selected in μ^- decay mode, while ES$^+$ sample is selected in μ^+ decay mode.

6.1.1 Calorimetric vertex selections

Both IMD and ES events have a property of low (consistent with single particle) energy deposition near the vertex. To exploit that, a cut on energy deposit in the vertex bar of 4 MeV is imposed. If vertex is in a cluster of fibers, a cut is made on its amplitude (the sum of fiber amplitudes). In some background events, energetic (hundreds of MeV) charged hadrons escape through the air gaps leaving small or no deposits in the calorimetric sections. Therefore, it is required that there is no activity in side bars covering air gaps adjacent to the vertex. Another vertex related cut is the requirement that there is no energy deposits upstream of the vertex (backward deposits). Distributions of energy deposit in the vertex bar and energy deposit in side slab for signal and background events are shown on Figure 6.1 and Figure 6.2.
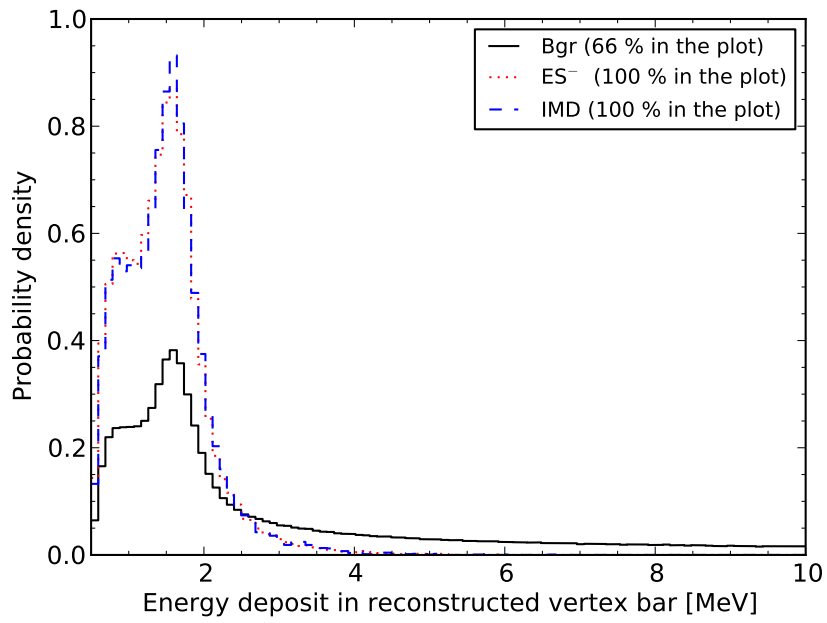
Figure 6.1: Distributions of energy deposit in vertex bar for IMD (blue), ES$^-$ (red) and background (black) events in μ^- mode. The fraction of events contained in the plot is indicated in the legend. All distributions are normalized to a unit area. This plot shows only events in which the reconstructed vertex volume is a bar.
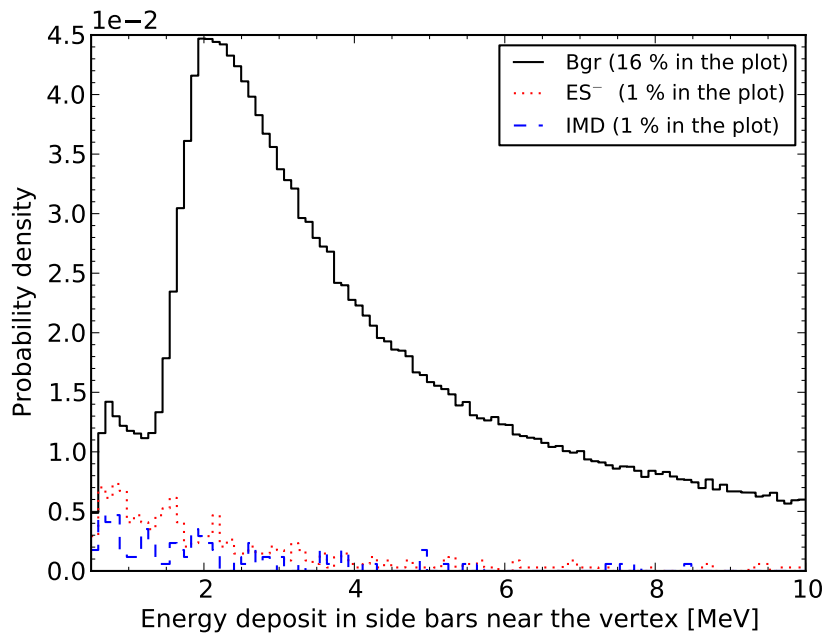
Figure 6.2: Distributions of total energy deposit in bars covering air gaps adjacent to the vertex for IMD (blue), ES$^-$ (red) and background (black) events in μ^- mode. The fraction of events contained in the plot is indicated in the legend. All distributions are normalized to a unit area.
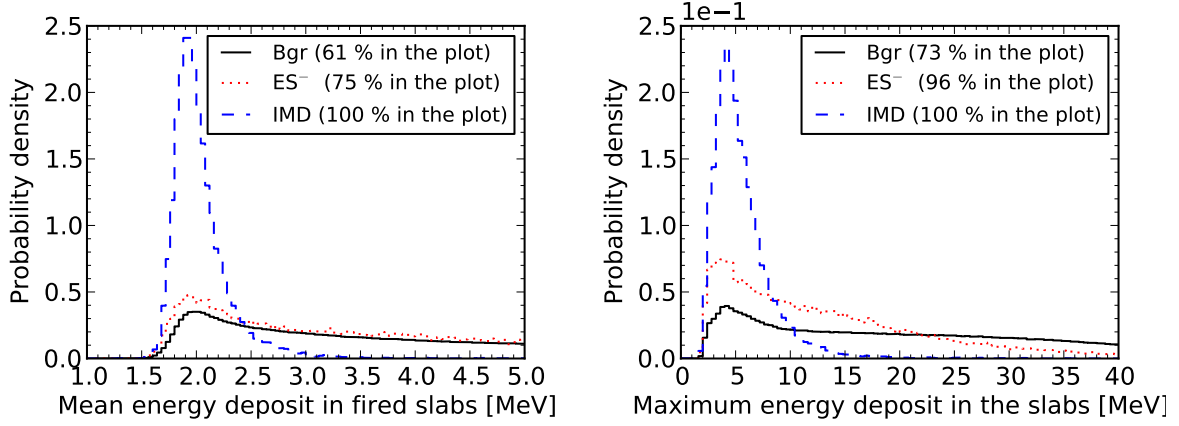
Figure 6.3: Distributions of $\langle \Delta E_i \rangle$ (left) and $max(\Delta E_i)$ (right) for IMD (blue), ES$^-$ (red) and background (black) events in μ^- mode. The fraction of events contained in the plot is indicated in the legend. All distributions are normalized to a unit area.

6.1.2 Other calorimetric selections

To select IMD events, one can rely on the specific properties of muon dE/dx. At energies in the range of 11-25 GeV, a muon is nearly a minimum ionizing particle. Therefore, the following cuts were applied when selecting IMD events: mean of all slab deposits $\langle \Delta E_i \rangle$ is less than 3 MeV and the maximum $max(\Delta E_i)$ is less than 12 MeV. For ES events, primary electron might induce shower in the detector, thus such cuts are not suitable. Signal and background distributions of $\langle \Delta E_i \rangle$ and $max(\Delta E_i)$ are shown on Figure 6.3. For selecting IMD events, the x_{dev} variable is cut at 2.5 cm, while for ES events a more relaxed cut at 15 cm is applied. Signal and background distribution of the x_{dev} variable are shown on Figure 6.4.

6.1.3 Kinematic selections

As signal events always have negatively charged primary lepton (μ^- or e$^-$), a cut $q/p < 0$ on the primary track is imposed. Quasi-elastic neutrino electron scattering has a threshold at ~ 11 GeV. Therefore, when selecting the IMD sample, events with primary track momenta of less than 10 GeV are discarded. In order to avoid contamination of IMD events in the ES$^-$ sample, only events with primary track momentum less than 10 GeV are retained in this sample.[1] This is a reasonable cut, since majority of ES$^-$ events

---

[1]A full containment calorimeter enclosing the detector will be able to distinguish electrons from muons with high confidence. However, such additional calorimeter is not envisaged in the current near
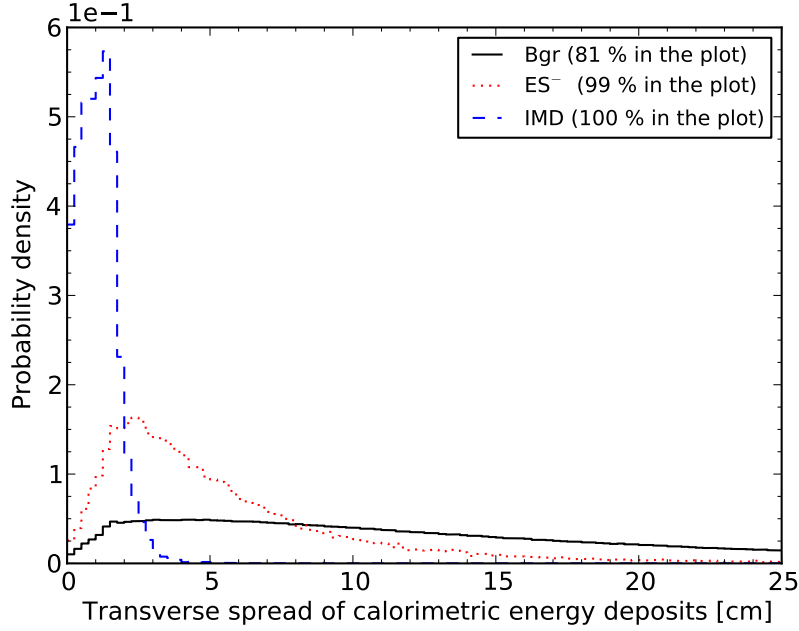
Figure 6.4: Distributions of the x_{dev} variable for IMD (blue), ES$^-$ (red) and background (black) events in μ^- mode. The fraction of events contained in the plot is indicated in the legend. All distributions are normalized to a unit area.

have primary track momentum of less than 10 GeV. Distributions of primary track's reconstructed q/p and momentum are shown on Figure 6.5.

The overall efficiencies of the selection cuts are 89 % for IMD sample, 73 % for ES$^-$ sample and 87 % for ES$^+$ sample. All cuts with their efficiency and purity[2] are summarized in Appendix A.

6.2 Background subtraction

Absolutely clean sample of signal events cannot be selected with a reasonable efficiency by employing selection cuts only. Therefore extrapolations of certain background distributions should be made in order to subtract background from event samples. Background subtraction is different from event selection in the sense that after it is done, one obtains a distribution of signal events and loses event by event information.

---

detector design and the author prefers not to make assumptions on electron/muon discriminating capabilities.

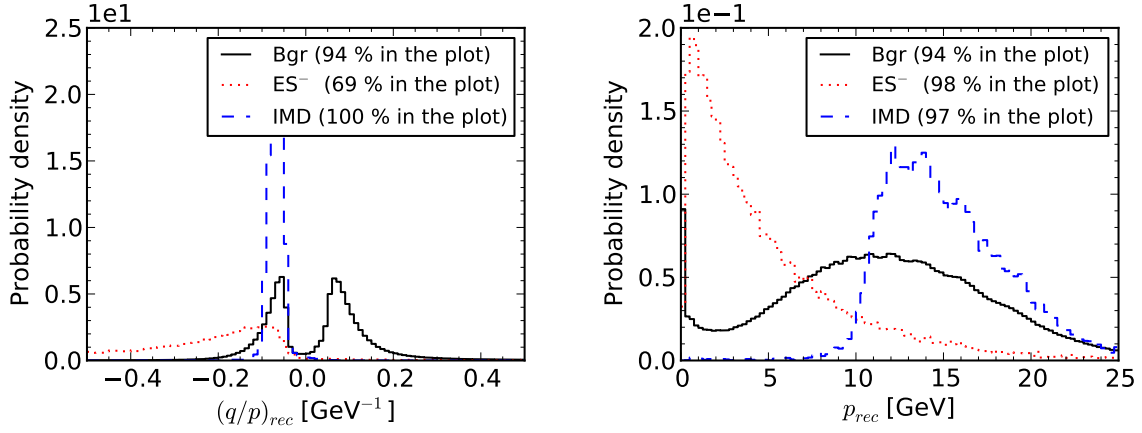[2]Purity is the ratio $\frac{N_{signal}}{N_{signal}+N_{background}}$.

Figure 6.5: Distributions of primary track reconstructed q/p (left) and momentum (right) for IMD (blue), ES$^-$ (red) and background (black) events in μ^- mode. The fraction of events contained in the plot is indicated in the legend. All distributions are normalized to a unit area.

We have chosen to do background subtraction in terms of primary lepton (μ or e) kinematic variables for the following reasons:

- they provide the most powerful signal/background separation criteria;

- background distributions can be most reliably extrapolated in terms of kinematic variables;

- we can reliably measure primary lepton angular and momentum resolutions.

The primary lepton's scattering angle θ_ℓ and initial momentum p are measured in the detector. Primary muons with energy above 1 GeV and all primary electrons are ultrarelativistic. Therefore, it is justified to approximate the primary lepton's initial energy with $E = pc$. For simplicity, we will perform one dimensional analysis, where histograms over a variable $x = f(\theta, p)$ will be used for background subtraction. In the case of IMD signal extraction, scattering angle θ_ℓ and $\theta_\ell^2 E_\ell$ variable (see Section 2.3) can be used to discriminate signal from background. In the case of ES signal, background is well separated only when one expoloits $\theta_\ell^2 E_\ell$ variable. The distributions of θ_ℓ and $\theta_\ell^2 E_\ell$ for IMD signal, ES$^-$ signal and background are shown on Figure 6.6. Background distribution over $\theta_\ell^2 E_\ell$ variable is nearly flat. This fact allows for a simple parameterization of the background distribution. Our further analysis is made using only $\theta_\ell^2 E_\ell$ variable.

As a first approximation we assume that the energy distribution of neutrinos in the beam is known. Then, by measuring only the number of signal events, one can make
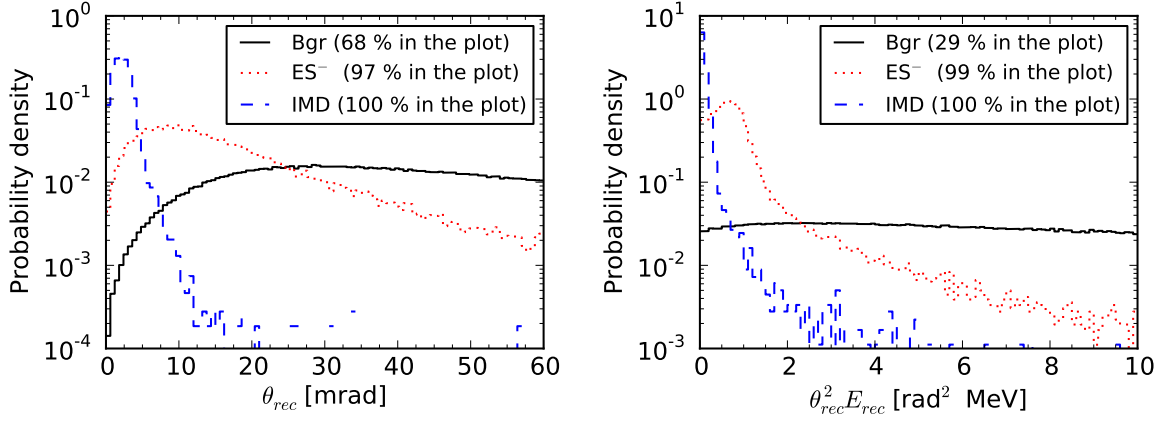
Figure 6.6: Distributions of reconstructed primary track initial angle θ_ℓ and $\theta_\ell^2 E_\ell$ variable for IMD (blue), ES$^-$ (red) and background (black) events in μ^- mode. The fraction of events contained in the plot is indicated in the legend. All distributions are normalized to a unit area.

absolute flux normalization. Two methods of obtaining the number of signal events are discussed below.

6.2.1 Linear fit method

Linear fit method relies on the nearly flat shape of the respective background distribution. The idea is to estimate the background under the signal peak by linear extrapolation from signal-free region. First, an interval on the $\theta_\ell^2 E_\ell$ variable is defined by the following rules:

- the interval low limit is close to the signal peak;

- there are almost no signal events in the interval (according to MC simulation);

- the background is approximately linear in the interval.

Then, the histogram is fitted with a straight line in the interval. Finally, the line is extrapolated towards zero to estimate the number of background events under the signal peak. The histograms over $\theta_\ell^2 E_\ell$ and the linear fits for the three event samples under consideration are shown in Figures 6.7, 6.8 and 6.9. Comparison between the estimated and the true number of signal events is given on Table 6.1. It is seen that the true values lie within the 95 % confidence intervals of the predictions. This means that the hypothesis that the predictions are unbiased cannot be excluded. The main source of
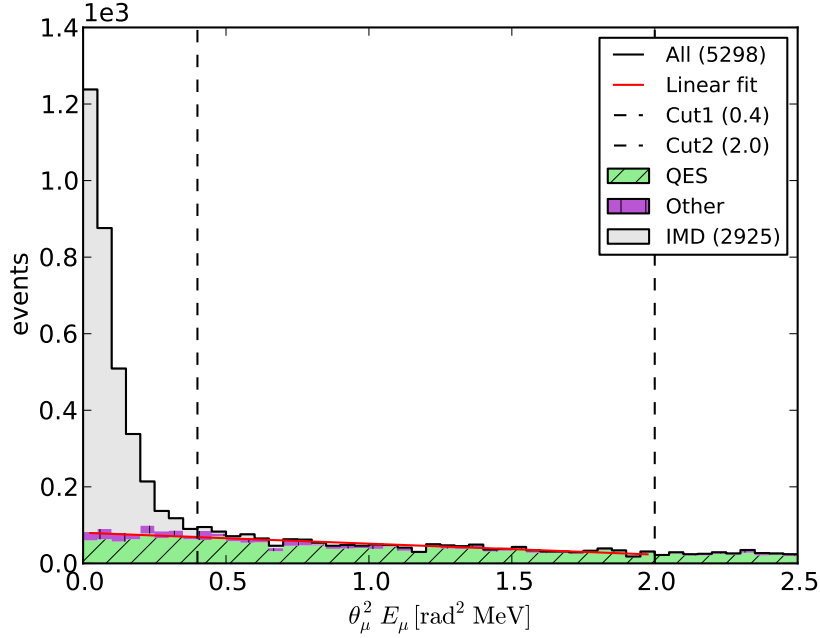
Figure 6.7: Distributions over $\theta_\mu^2 E_\mu$ for the IMD sample. The leptonic events histogram is filled with solid gray, the hadronic events histogram is hatched and the total spectrum is in black. The two cuts bounding the fit interval are drawn with dashed line. The red line indicates the background extrapolation.

systematic error related to the method is the assumption about the linearity of the background shape. From the fit of the ES$^-$ and ES$^+$ samples it is estimated that the systematic error of the method

$$\Delta_{syst} = \frac{|N_{fit}^{sig} - N_{true}^{sig}|}{N_{true}^{sig}}, \tag{6.1}$$

is less than 1 %. However, to give conclusive estimation of the systematic error, one should investigate if and how various parameters of simulation and selections influence the background shape.

6.2.2 μ^+-method

IMD interactions are present only in the μ^- decay mode. The idea of the μ^+-method is to estimate the background under the IMD signal peak exploiting the distribution of positive muons detected in $(\overline{\nu}_\mu, \nu_e)$-beam. The idea was previously used for measuring IMD process in the CHARM II detector [19, 20]. In the near detector, an event sample
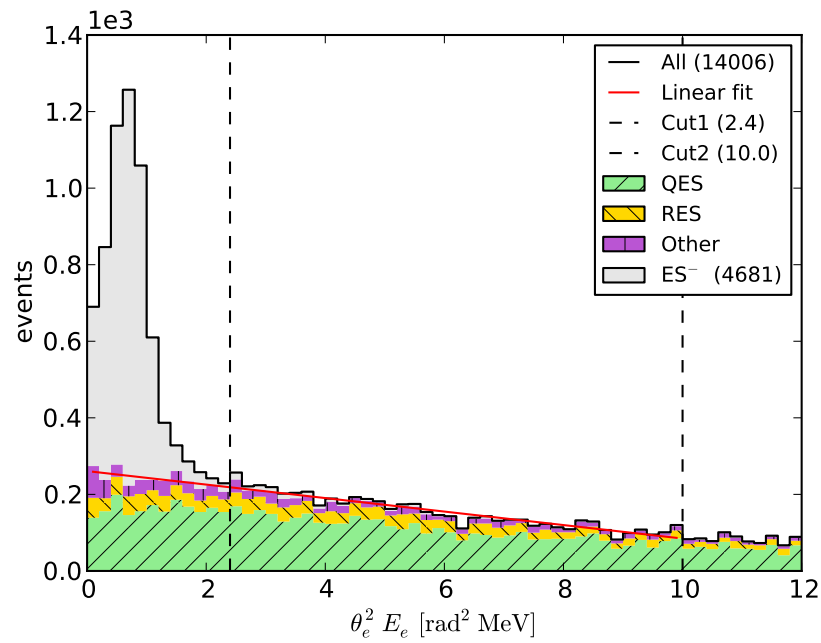
Figure 6.8: Distributions over $\theta_e^2 E_e$ for the ES$^-$ sample. The leptonic events histogram is filled with solid gray, the hadronic events histogram is hatched and the total spectrum is in black. The two cuts bounding the fit interval are drawn with dashed line. The red line indicates the background extrapolation.

Figure 6.9: Distributions over $\theta_{\mathrm{e}}^2 E_{\mathrm{e}}$ for the ES$^+$ sample. The leptonic events histogram is filled with solid gray, the hadronic events histogram is hatched and the total spectrum is in black. The two cuts bounding the fit interval are drawn with dashed line. The red line indicates the background extrapolation.
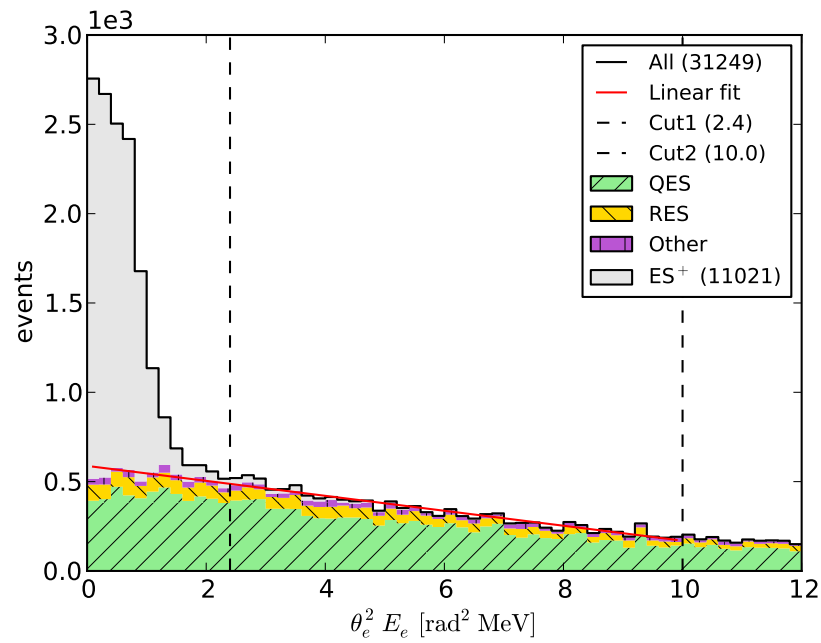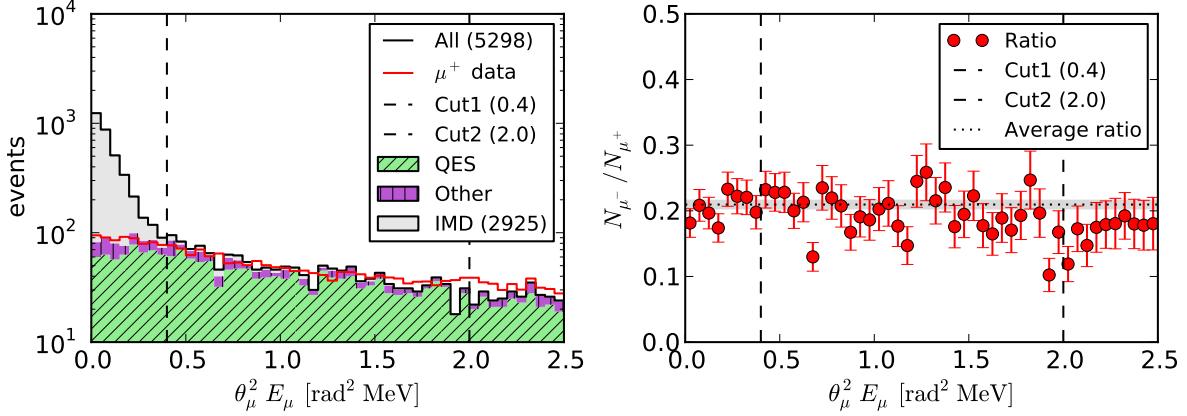
Figure 6.10: Left plot shows distributions over $\theta_\mu^2 E_\mu$ for the IMD sample. The leptonic events histogram is filled with solid gray, the hadronic events histogram is hatched and the total spectrum is in black. The two cuts bounding the normalization interval Δ are drawn with dashed line. The red line indicates the normalized μ^+ histogram. Right plot shows ratio of the μ^- histogram and the μ^+ histogram over $\theta_\mu^2 E_\mu$. The errors are statistical and bars correspond to 1σ. Horizontal dotted line indicates the normalization ratio.

from the $(\overline{\nu}_\mu, \nu_e)$-beam events is selected with the same selection cuts as the IMD sample. For consistency, we again consider the $\theta_\mu^2 E_\mu$ distributions. Muon antineutrino inclusive CC interactions $\overline{\nu}_\mu N$ have approximately twice higher cross section than $\nu_\mu N$ interactions. To account for that, the $\theta_\mu^2 E_\mu$ histogram for μ^+ should be normalized to the $\theta_\mu^2 E_\mu$ histogram for μ^-. First, the ratio of the μ^- background histogram and the μ^+ histogram is calculated - Figure 6.10 (right). It is seen, that the ratio under the signal peak ($\theta_\mu^2 E_\mu < 0.4$ rad²MeV) is at the same level as the ratio outside the signal peak. An interval outside the IMD signal peak and with approximately constant ratio of μ^-- and μ^+-events is defined: $\Delta = [0.4, 2.0]$ rad²MeV. The normalization factor is then

$$R = \frac{N_{\mu^-}^\Delta}{N_{\mu^+}^\Delta} = 0.210 \pm 006, \tag{6.2}$$

where $N_{\mu^-}^\Delta$ ($N_{\mu^+}^\Delta$) is the number of events in the interval Δ for the μ^- (μ^+) histogram. The μ^- histogram and the normalized μ^+ histogram are shown in Figure 6.10 (left). Apart from normalization, there are second order differences between μ^- and μ^+ distributions [19, 20], which are not taken into account.

Table 6.1: Estimated number of signal events for the three event samples. The result in the last row was obtained using the μ^+ background subtraction method, while the other three results were obtained using linear fit background subtraction method. Statistics correspond to 2.3×10^{19} μ^- decays and 2.3×10^{19} μ^+ decays, which is approximately a tenth of the nominal year.

Event sample	Selection eff.	Overall eff.	Purity	All events	Signal events	Signal events from fit
IMD	86 %	46 %	81 %	3520	2850	2926 $\pm$ 59
ES$^-$	70 %	32 %	61 %	7355	4491	4479 $\pm$ 86
ES$^+$	83 %	37 %	63 %	16964	10607	10512 $\pm$ 131
IMD	86 %	46 %	81 %	3520	2850	2831 $\pm$ 61

Chapter 7

Conclusions

We have proposed a conceptual design for the tracker part of the Neutrino Factory near detector. A full Monte Carlo simulation of neutrino interactions and particle transport was implemented using standard tools. An idealized detector geometry and simplified signal digitization was used in the MC simulation. Basic reconstruction algorithms were developed to extract information relevant for neutrino-electron scattering measurements. Selection procedures, which increase signal to background ratio from $\sim 10^{-4}$ initially to $\sim$ 30-50 %, are defined. One dimensional signal extraction analysis was performed. It is demonstrated that the number of neutrino-electron scattering events can be measured from the $\theta_\ell^2 E_\ell$ variable histogram. A direct comparison between measured and true number of signal events shows a deviation of no more than 1 %. It is worth noting that MC truth was not used in reconstruction and signal extraction. Therefore, the results obtained in this work are a reliable approximation to results obtainable at a real experiment, provided that MC simulation is close to reality.

Further developments of the methods used towards a conclusive statement about the achievable precision of neutrino flux measurement are needed. A two-dimensional signal extraction procedure in the (θ_ℓ, p_ℓ) plane will allow the extraction of lepton energy distribution of signal events. Subsequently, a distribution of neutrino energy should be obtained. Development of advanced pattern recognition and fitting reconstruction algorithms is expected to improve on background rejection and angular and momentum resolutions. Finally, a dedicated analysis of systematic uncertainties should be made to asses the precision of the neutrino flux determination.

Appendix A

Summary of cuts

Tables A.1, A.2 and A.3 summarize the selection cuts for the IMD, ES$^-$ and ES$^+$ signal event samples. Only the efficiencies of the selection cuts (not including reconstruction efficiency) are given.

Table A.1: Selection cuts for the IMD sample.

Cut		Eff. after cut	Purity after cut
All events in detector			0.85×10^{-4}
Reconstruction selections			0.19 %
Side slabs deposit	$= 0$ MeV	99 %	0.25 %
Backward deposit	$= 0$ MeV	98 %	0.28 %
Vertex deposit	< 4 MeV or		
	< 500 p.e.	98 %	0.47 %
$\langle \Delta E_i \rangle$	< 3 MeV	96 %	1.4 %
$\max(\Delta E_i)$	< 12 MeV	94 %	1.5 %
x_{dev}	< 2.5 cm	92 %	13 %
$(q/p)_{rec}$	< 0	91 %	28 %
p_{rec}	> 10 GeV	89 %	34 %

Table A.2: Selection cuts for the ES$^-$ sample.

Cut		Eff. after cut	Purity after cut
All events in detector			2.0×10^{-4}
Reconstruction selections			0.37 %
Side slabs deposit	$= 0$ MeV	98 %	0.48 %
Backward deposit	$= 0$ MeV	95 %	0.52 %
Vertex deposit	< 4 MeV or		
	< 500 p.e.	94 %	0.89 %
x_{dev}	< 15 cm	89 %	1.5 %
$(q/p)_{rec}$	< 0	86 %	7.2 %
p_{rec}	< 10 GeV	73 %	23 %

Table A.3: Selection cuts for the ES$^+$ sample.

Cut		Eff. after cut	Purity after cut
All events in detector			4.1×10^{-4}
Reconstruction selections			0.67 %
Side slabs deposit	$= 0$ MeV	98 %	0.83 %
Backward deposit	$= 0$ MeV	95 %	0.89 %
Vertex deposit	< 4 MeV or		
	< 500 p.e.	94 %	1.4 %
x_{dev}	< 15 cm	90 %	2.2 %
$(q/p)_{rec}$	< 0	87 %	24 %

Acknowledgements

Bibliography

[1] S. Choubey *et al.*, "International Design Study for the Neutrino Factory, Interim Design Report,". IDS-NF-20,
`https://www.ids-nf.org/wiki/FrontPage/Documentation/IDR`.

[2] K. T. McDonald *et al.*, "The MERIT High-Power Target Experiment at the CERN PS," in *Proceedings of IPAC'10, Kyoto, Japan*, pp. 3527–3529. 2010.
`http://accelconf.web.cern.ch/AccelConf/IPAC10/papers/wepe078.pdf`.

[3] Y. Karadzhov, "Status of MICE, the international Muon Ionisation Cooling Experiment," *PoS* **ICHEP2010** (2010) 323.
`http://pos.sissa.it/cgi-bin/reader/conf.cgi?confid=120`.

[4] **T2K Collaboration** Collaboration, Y. Oyama, "Current status of the T2K experiment," `arXiv:1108.4457 [hep-ex]`.

[5] Л. Б. Окунь, *Лептоны и кварки*, 2-е изд., Москва, Наука, 1990.

[6] W. J. Marciano and Z. Parsa, "Neutrino electron scattering theory," *J. Phys. G* **G29** (2003) 2629–2645, `arXiv:hep-ph/0403168 [hep-ph]`.

[7] **Particle Data Group** Collaboration, K. Nakamura *et al.*, "Review of particle physics," *J. Phys.* **G37** (2010) 393.

[8] Z. Sadygov, 1996. Russian patent No. 2102820.

[9] N. Bacchetta *et al.*, "New type of metal-resistive layer-silicon avalanche detectors for visible and UV light detection," *Nucl. Instrum. Meth.* **A383** (1996) 263–265.

[10] Y. Karadzhov, "Neutrino Factory Near Detector Simulation," *AIP Conf. Proc.* **1222** (2010) 467–470. `http://link.aip.org/link/?APCPCS/1222/467/1`.

[11] Y. Karadzhov and R. Tsenov, "Neutrino Factory Near Detector Simulation," *Annual of University of Sofia, Faculty of Physics* **103** (2010) .

http://phys.uni-sofia.bg/annual/arch/103/arch_en.html.

[12] **Particle Data Group** Collaboration, K. Nakamura *et al.*, "Review of particle physics," *J. Phys.* **G37** (2010) 521–523.

[13] C. Andreopoulos *et al.*, "The GENIE Neutrino Monte Carlo Generator," *Nucl. Instrum. Methods* **A614** (2010) 87–104, `arXiv:0905.2517 [hep-ph]`.

[14] **GEANT4** Collaboration, S. Agostinelli *et al.*, "GEANT4: A simulation toolkit," *Nucl. Instrum. Methods* **A506** (2003) 250–303.

[15] J. Allison, K. Amako, J. Apostolakis, H. Araujo, P. Dubois, *et al.*, "Geant4 Developments and Applications," *IEEE Trans. Nucl. Sci.* **53** (2006) 270.

[16] D. H. Wright, "Simple and Fast Physics List for GEANT4.". `http://www.slac.stanford.edu/comp/physics/geant4/slac_physics_lists/simple/simple_physics_list.html`.

[17] Z. Papandreou, "Scintillating fiber trapping efficiency." `http://argus.phys.uregina.ca/cgi-bin/public/DocDB/ShowDocument?docid=918`.

[18] R. E. Kalman, "A new approach to linear filtering and prediction problems," *Transactions of the ASME–Journal of Basic Engineering* **D82** (1960) 35–45.

[19] **CHARM-II** Collaboration, D. Geiregat *et al.*, "A New measurement of the cross-section of the inverse muon decay reaction $\nu_\mu + e^- \to \mu^- + \nu_\mu$," *Phys. Lett.* **B247** (1990) 131–136.

[20] **CHARM-II** Collaboration, P. Vilain *et al.*, "A Precise measurement of the cross-section of the inverse muon decay $\nu_\mu + e^- \to \mu^- + \nu_\mu$," *Phys. Lett.* **B364** (1995) 121–126.